

# Linear and Cubic Box Splines for the Body Centered Cubic Lattice

Alireza Entezari

Ramsay Dyer

Torsten Möller \*

Graphics, Usability, and Visualization (GrUVi) Lab, Simon Fraser University

## Abstract

In this paper we derive piecewise linear and piecewise cubic box spline reconstruction filters for data sampled on the body centered cubic (BCC) lattice. We analytically derive a time domain representation of these reconstruction filters and using the Fourier slice-projection theorem we derive their frequency responses. The quality of these filters, when used in reconstructing BCC sampled volumetric data, is discussed and is demonstrated with a raycaster. Moreover, to demonstrate the superiority of the BCC sampling, the resulting reconstructions are compared with those produced from similar filters applied to data sampled on the Cartesian lattice.

**CR Categories:** G.1.1 [Numerical Analysis]: Approximation—Box Splines; G.1.2 [Numerical Analysis]: Interpolation—Box Splines

**Keywords:** Body Centered Cubic Lattice, Reconstruction, Optimal Regular Sampling

## 1 Introduction

With the advent of the theory of digital signal processing various fields in science and engineering have been dealing with the discrete representations of (assumably) continuous phenomena. As scientific computing algorithms mature and find applications in a spectrum of scientific, medical and engineering fields, the question of the accuracy of the discrete representations gains an enormous importance. The theory of optimal sampling deals with this issue: given a fixed number of samples, how can one capture the most amount of information possible from the underlying continuous phenomena; hence, such a sampling pattern would constitute the most accurate discrete representation.

The study of optimal regular sampling patterns is not new [8, 17, 13]. If we are considering an object (or signal) with a spherically uniform spectrum (i.e. no preferred direction of resolution), the problem of optimal regular sampling can be answered using the solution to the optimal sphere packing problem. This is due to the fact that the sparsest regular (lattice) distribution of samples in the spatial domain demands the tightest arrangement of the replicas of the spectrum in the Fourier domain. Therefore, the optimal sampling lattice is simply the dual lattice of the densest sphere packing lattice.

The sphere packing problem [6] can be traced back to the early 17th century. Finding the densest packing of spheres is known as the Kepler problem. The fact that the face centered cubic (FCC) packing attains the highest density of lattice packings was first proven by Gauß in 1831 [6].

Further, the Kepler conjecture – that the FCC packing is an optimal packing of spheres in 3D even when the lattice condition is not imposed – was not proven until 1998 by a lengthy computer-aided proof [9].

While the optimal regular sampling theory is attractive for its theoretical advantages, it hasn't been widely employed in practice due to the lack of signal processing theory and tools to handle such a sampling lattice. This paper makes a significant contribution in order to overcome this problem by designing box spline reconstruction filters for the body-centered cubic lattice (BCC), the dual of the FCC lattice.

An introduction to multi-dimensional sampling theory can be found in Dudgeon and Mersereau [8]. A lattice can be viewed as a periodic sampling pattern. Periodic sampling of a function in the spatial domain gives rise to a periodic replication of the spectrum in the Fourier domain. The lattice that describes the centers of the replicas in the Fourier domain is called the *dual*, *reciprocal*, or *polar* lattice. The reconstruction in the spatial domain amounts to eliminating the replicas of the spectrum in the Fourier domain and preserving the primary spectrum. Therefore, the ideal reconstruction function is the inverse Fourier transform of the characteristic function of the Voronoi cell of the dual lattice.

## 2 Literature Review

The design of reconstruction filters is a very rich area of signal processing and approximation theory. The literature in the domain of signal processing typically uses constraints in the Fourier Domain in order to guide the filter design process (see e.g. [1, 19, 3]), which often results in discrete filter weights (or “taps”). These filters resample a given regular sampling pattern on a new regular sampling pattern. Approaches from approximation theory often use constraints in the spatial domain in order to design continuous filters, that allow the reconstruction of samples with arbitrary offset from the given sampling lattice ([18, 14, 16]).

While all these design approaches yield one-dimensional filters, in the areas of image processing and volume rendering we need to interpolate higher-dimensional functions. The common approach is to design the filter in one dimension and then to extend the filter into higher dimensions through a separable extension (tensor product) or through a spherical extension. While separable extensions are justified due to the separability of the sampling lattice, spherical extensions often suffer from the fact that it is difficult to guarantee zero-crossings of the filter at all replicas of the frequency response. These problems of spherical extensions remain in all sampling lattices. If we are dealing with optimal sampling patterns, a separable extension cannot be applied, since the sampling lattice itself is not separable.

The use of optimal sampling in image processing is limited, due to the overhead of dealing with the hexagonal lattice and the possibly small efficiency gain of 13%. However, Van De Ville et al. [21] recently presented a B-spline family of interpolation filters for 2D hexagonally sampled data. They describe the Voronoi cell of the sampling lattice,

\*e-mail:{aentezar,rhdyer,torsten}@cs.sfu.ca

which is a hexagon, in terms of superposition of building block functions. These functions can be described in the Fourier domain analytically. They formulate their hexagonal B-spline family in terms of successive convolutions of these functions.

In volume graphics optimality of BCC sampling has been explored and demonstrated by Theußl et al. [11]. However, spherical extension of interpolation filters as used in that paper resulted in rather blurry and unsatisfying results. Theußl et al [10] have studied different ad-hoc approaches for reconstruction and derivative reconstruction on BCC lattices with mixed results. Also isosurface extraction on the optimal sampling lattice has been studied with inconclusive results [5, 4].

In order to exploit the theoretical optimality of the BCC lattice, reconstruction filters are needed with proven zero crossings of the frequency response at all replicas of the spectrum. To the best knowledge of the authors no BCC interpolation filters have yet been proposed which can be rigorously shown to possess these properties. We will see that with the methods developed in this paper, the predicted theoretical advantages of BCC lattices can be demonstrated in practice.

### 3 The BCC Lattice

A *lattice* is defined as an infinite array of points in which each point has surroundings identical to those of all the other points [2]. In other words, every lattice point has the same Voronoi cell and we can refer to the Voronoi cell of the lattice without ambiguity. The lattice points form a group under vector addition in the Euclidean space. A lattice can be represented by a matrix that gathers a set of basis vectors, indexing the lattice points, into columns. The BCC lattice is a sub-lattice of the Cartesian lattice. The BCC lattice points are located on the corners of the cube with an additional sample in the center of the cube as illustrated in Figure 1. An alternative way of describing the BCC lattice is to start with a Cartesian lattice (i.e.  $\mathbb{Z}^3$ ) and retain only those points whose coordinates have identical parity.

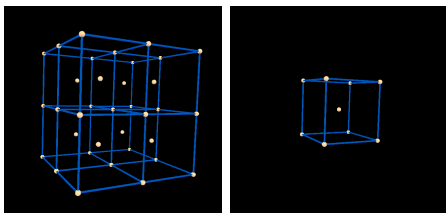


Figure 1: The BCC Lattice

The simplest interpolation kernel on any lattice is the characteristic function of the Voronoi cell of the lattice. This is usually called nearest neighbor interpolation. More sophisticated reconstruction kernels involve information from the neighboring points of a given lattice point. With this in mind, we focus in the next section on the geometry and the polyhedra associated with the BCC lattice.

#### 3.1 Polyhedra Associated with the BCC Lattice

Certain polyhedra arise naturally in the process of constructing interpolation filters for a lattice. The Voronoi cell of the lattice is one such example. The Voronoi cell of the Cartesian lattice is a cube and the Voronoi cell of the BCC lattice is a truncated octahedron as illustrated in Figure 2a.

We are also interested in the cell formed by the nearest neighbors of a lattice point. The first neighbors of a lattice point are defined by the Delaunay tetrahedralization of the lattice; a point  $q$  is a *nearest neighbor* of  $p$  if their respective Voronoi cells share a (non-degenerate) face. The *first neighbors cell* is the polyhedron whose vertices are the first neighbors. Again, this cell is the same for all points on the lattice.

For example, by this definition there are six first neighbors of a point in a Cartesian lattice; the first neighbors cell for the Cartesian lattice is the octahedron. For the BCC lattice there are fourteen first neighbors for each lattice point that form a rhombic dodecahedron that is illustrated in Figure 2b.

The geometry of the dual lattice is of interest when we consider the spectrum of the function captured by the sampling operation. The Cartesian lattice is self dual. However, the dual of the BCC lattice is the FCC lattice. The FCC lattice is a sublattice of  $\mathbb{Z}^3$  and it is often referred to as  $D_3$  lattice [6]. The general  $D_n$  family of lattices are sometimes called checkerboard lattices. The checkerboard property implies that the sum of the coordinates of the lattice sites is always even. We will use this property to demonstrate the zero crossings of the frequency response of the reconstruction filters at the FCC lattice sites. The Voronoi cell of the FCC lattice is the rhombic dodecahedron as illustrated in Figure 2c whose characteristic function is the frequency response of the ideal reconstruction filter for the BCC lattice. Figure 2d shows the first neighbors cell of the FCC lattice; the cuboctahedron.

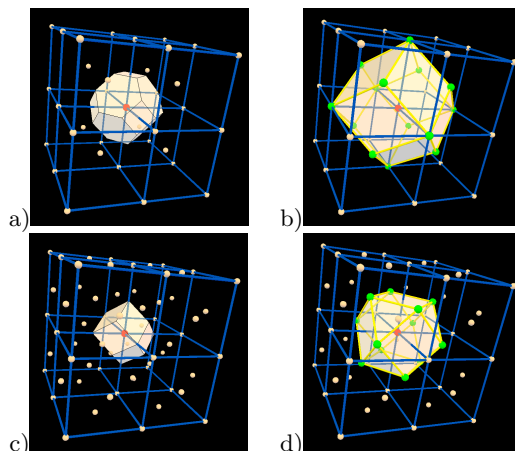


Figure 2: The Voronoi cell of the BCC lattice is the truncated octahedron (a), and its first neighbor cell is the rhombic dodecahedron (b). For the FCC lattice, the rhombic dodecahedron is the Voronoi cell (c), and the cuboctahedron is the first neighbor cell (d).

### 4 Reconstruction Filters

The nearest neighbor interpolation kernel in 1D is the Box function. It is the characteristic function of the Voronoi cell of the samples on the real line. The nearest neighbor interpolation on the BCC lattice is similarly defined in terms of the Voronoi cell of the lattice which is a truncated octahedron (Figure 2(a)). In this scheme, a point in space is assigned the value of the sample in whose Voronoi cell it is located. Since the Voronoi cell tiles the space, its characteristic function induces an interpolation scheme for that lattice. Based on the fact that the periodic tiling of the Voronoi cell yields the

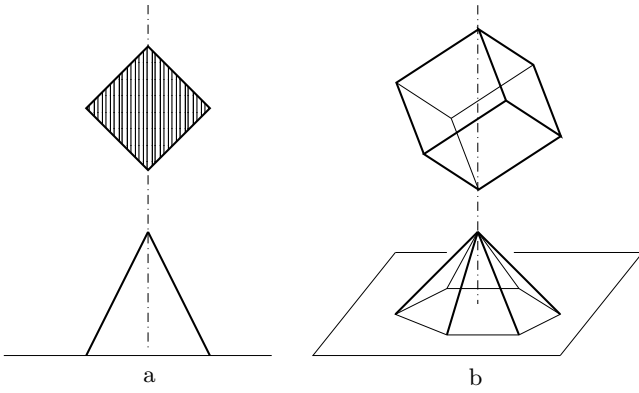


Figure 3: a) one dimensional linear box spline (Triangle function). b) the two dimensional hexagonal linear box spline

constant function in the spatial domain, Van De Ville [21] proves by means of the Poisson summation formula that the frequency response of such a kernel does in fact vanish at the aliasing frequencies.

#### 4.1 Linear Box Spline

DeBoor et al [7] analytically define the box splines, in  $n$ -dimensional space, by successive directional convolutions. They also describe an alternative geometric description of the box splines in terms of the projection of higher dimensional boxes ( $nD$  cubes). A simple example of a one dimensional linear box spline is the triangle function which can be obtained by projecting a 2D box along its diagonal axis down to 1D. The resulting function (after proper scaling) is one at the origin and has a linear fall off towards the first neighbors as illustrated in Figure 3a.

The properties and behaviors of box splines are studied in [7]. For example, the order of the box splines can be determined in terms of the difference in dimension between the higher dimensional box and the lower dimensional projection. For instance, the triangle function is a projection of a 2D cube into 1D, hence it is a first order box spline.

Our construction of box splines for the BCC lattice is guided by the fact that the rhombic dodecahedron (the first neighbors cell of the BCC lattice) is the three-dimensional shadow of a four-dimensional hypercube (tesseract) along its antipodal axis. This fact will be revealed in the following discussion. This construction is reminiscent of constructing a hexagon by projecting a three-dimensional cube along its antipodal axis; see Figure 3b.

Integrating a constant tesseract of unit side length along its antipodal axis yields a function that has a rhombic dodecahedron support (see Figure 3b), has the value two<sup>1</sup> at the center and has a linear fall off towards the fourteen first neighbor vertices. Since it arises from the projection of a higher dimensional box, this filter is the first order (linear) box spline interpolation filter on the BCC lattice.

Let  $\mathcal{B}$  denote the Box distribution. The characteristic function of the unit tesseract is given by a product of these functions:

$$T(x, y, z, w) = \mathcal{B}(x) \mathcal{B}(y) \mathcal{B}(z) \mathcal{B}(w). \quad (1)$$

<sup>1</sup>Note that the BCC sampling lattice has a sampling density of two samples per unit volume.

Let  $\mathbf{v} = \langle 1, 1, 1, 1 \rangle$  denote a vector along the antipodal axis. In order to project along this axis, it is convenient to rotate it so that it aligns with the  $w$  axis. Let

$$\mathbf{R} = \frac{1}{2}[\boldsymbol{\rho}_1 \boldsymbol{\rho}_2 \boldsymbol{\rho}_3 \boldsymbol{\rho}_4] = \frac{1}{2} \begin{bmatrix} -1 & -1 & 1 & 1 \\ -1 & 1 & -1 & 1 \\ 1 & -1 & -1 & 1 \\ 1 & 1 & 1 & 1 \end{bmatrix} \quad (2)$$

This rotation matrix transforms  $\mathbf{v}$  to  $\langle 0, 0, 0, 2 \rangle$ .<sup>2</sup> Let  $\mathbf{x} = \langle x, y, z, w \rangle$ ; now the linear kernel is given by

$$L_{RD}(x, y, z) = \int \mathcal{T}(\mathbf{R}^T \mathbf{x}) dw.$$

Substituting in equation (1) we get

$$L_{RD}(x, y, z) = \int \prod_{i=1}^4 \mathcal{B}\left(\frac{1}{2} \boldsymbol{\rho}_i \cdot \mathbf{x}\right) dw. \quad (3)$$

We illustrate an analytical evaluation of this integral in Section 5.

#### 4.2 Cubic Box Spline

By convolving the linear box spline filter kernel with itself we double its vanishing moments in the frequency domain. Hence the result of such an operation will have a cubic approximation order [20]. As noted by de Boor [7], the convolution of two box splines is again a box spline.

An equivalent method of deriving this function would be to convolve the tesseract with itself and project the resulting distribution along a diagonal axis (this commutation of convolution and projection is easy to understand in terms of the corresponding operators in the Fourier domain – see Section 4.3). Convolution of a tesseract with itself results in another tesseract which is the tensor product of four one-dimensional triangle functions.

Let  $\Lambda$  denote the triangle function. Then convolving the characteristic function of the tesseract yields

$$\mathcal{T}_c(x, y, z, w) = \Lambda(x) \Lambda(y) \Lambda(z) \Lambda(w). \quad (4)$$

Following the same 4D rotation as in the previous section, we obtain a time domain representation of the cubic box spline filter kernel:

$$C_{RD}(x, y, z) = \int \prod_{i=1}^4 \Lambda\left(\frac{1}{2} \boldsymbol{\rho}_i \cdot \mathbf{x}\right) dw. \quad (5)$$

Again, we will illustrate in Section 5 how to evaluate this integral analytically.

#### 4.3 Frequency Response

From the construction of the rhombic dodecahedron discussed earlier, we can analytically derive the frequency response of the linear function described by equation (3).

From equation (1), it is evident that the frequency domain representation of the characteristic function of the tesseract is given by the product of four sinc functions:

$$\tilde{T}(\omega_x, \omega_y, \omega_z, \omega_w) = \text{sinc}(\omega_x) \text{sinc}(\omega_y) \text{sinc}(\omega_z) \text{sinc}(\omega_w).$$

<sup>2</sup>By examining equation (2), one can see that each vertex of the rotated tesseract, when projected along the  $w$  axis, will coincide with the origin or one of the vertices of the rhombic dodecahedron:  $\langle \pm \frac{1}{2}, \pm \frac{1}{2}, \pm \frac{1}{2} \rangle$ ,  $\langle \pm 1, 0, 0 \rangle$ ,  $\langle 0, \pm 1, 0 \rangle$  or  $\langle 0, 0, \pm 1 \rangle$ .

While in the previous section the origin was assumed to be at the corner of the tesseract, for the simplicity of derivation, we now consider a tesseract whose center is at the origin. The actual integral, computed in Equation 3 or Equation 5 will not change.

By the Fourier slice-projection theorem, projecting the tesseract in the spatial domain is equivalent to slicing  $\tilde{T}$  perpendicular to the direction of projection. This slice runs through the origin. Again we make use of the rotation (2) to align the projection axis with the  $w$  axis. Thus in the frequency domain we take the slice  $\omega_w = 0$ .

It is convenient to introduce the  $3 \times 4$  matrix

$$\Xi = \frac{1}{2}[\xi_1 \xi_2 \xi_3 \xi_4] = \frac{1}{2} \begin{bmatrix} -1 & -1 & 1 & 1 \\ -1 & 1 & -1 & 1 \\ 1 & -1 & -1 & 1 \end{bmatrix} \quad (6)$$

given by the first three rows of the rotation matrix  $\mathbf{R}$  of equation (2). The frequency response of the linear kernel can now be written as

$$\tilde{L}_{RD}(\omega_x, \omega_y, \omega_z) = \prod_{i=1}^4 \text{sinc}\left(\frac{1}{2}\xi_i \cdot \omega\right), \quad (7)$$

where  $\omega = \langle \omega_x, \omega_y, \omega_z \rangle$ .

The box spline associated with this filter is represented by the  $\Xi$  matrix. The properties of this box spline can be derived based on this matrix according to the theory developed in [7]. For instance, one can verify  $C^0$  smoothness of this filter using  $\Xi$ .

We can verify the zero crossings of the frequency response at the aliasing frequencies on the FCC lattice points. Due to the checkerboard property for every  $\omega$  on the FCC lattice,  $\xi_4 \cdot \omega = (\omega_x + \omega_y + \omega_z) = 2k$  for  $k \in \mathbb{Z}$ ; therefore,  $\text{sinc}\left(\frac{1}{2}\xi_4 \cdot \omega\right) = 0$  on all of the aliasing frequencies. Since  $\xi_4 \cdot \omega = -\xi_1 \cdot \omega - \xi_2 \cdot \omega - \xi_3 \cdot \omega$ , at least one of the  $\xi_i \cdot \omega$  for  $i = 1, 2, 3$  needs to be also an even integer and for such  $i$  we have  $\text{sinc}\left(\frac{1}{2}\xi_i \cdot \omega\right) = 0$ ; therefore, there is a zero of order at least two at each aliasing frequency, yielding a  $C^0$  filter.

The cubic box spline filter can be similarly derived by projecting a tesseract composed of triangle functions. Again, the frequency response can be obtained via the Fourier slice-projection theorem.

Since convolution in one domain equals multiplication in the other domain, the frequency response of (4) is

$$\tilde{T}_c(\omega_x, \omega_y, \omega_z, \omega_w) = \text{sinc}^2(\omega_x) \text{sinc}^2(\omega_y) \text{sinc}^2(\omega_z) \text{sinc}^2(\omega_w).$$

By rotating and taking a slice as before we obtain:

$$\tilde{C}_{RD}(\omega_x, \omega_y, \omega_z) = \prod_{i=1}^4 \text{sinc}^2\left(\frac{1}{2}\xi_i \cdot \omega\right). \quad (8)$$

We can see that the vanishing moments of the cubic kernel are doubled from the linear kernel. We could also have obtained Equation 8 by simply multiplying Equation 7 with itself, which corresponds to convolving the linear 3D kernel with itself in the spatial domain.

The box spline matrix for the cubic kernel is  $\Xi' = [\Xi|\Xi]$ . One can verify the  $C^2$  continuity of this box spline using  $\Xi'$  and the theory in [7].

## 5 Implementation

In this section we describe a method to evaluate the linear and the cubic kernel analytically.

Let  $\mathcal{H}$  denote the Heaviside distribution. Using the fact that  $\mathcal{B}(x) = \mathcal{H}(x) - \mathcal{H}(x-1)$  we can expand the integrand of the linear kernel (Equation 3) in terms of Heaviside distributions. After simplifying the product of four Box distributions in terms of  $\mathcal{H}$ , we get sixteen terms in the integrand. Each term in the integrand is a product of four Heaviside distributions. Since  $x, y, z$  are constants in the integral and the integration is with respect to  $w$ , we group the  $x, y, z$  argument of each  $\mathcal{H}$  and call it  $t_i$ , using the fact that  $\mathcal{H}\left(\frac{1}{2}x\right) = \mathcal{H}(x)$ , we can write each term in the integrand as:

$$I = \int_a^b \mathcal{H}(w+t_0) \mathcal{H}(w+t_1) \mathcal{H}(w+t_2) \mathcal{H}(w+t_3) dw.$$

The integrand is non-zero only when all of the Heaviside distributions are non-zero and since the integrand will be constant one we have:

$$I = \max(0, b - \max(a, \max(-t_i))).$$

Similarly, for the cubic kernel in Equation 5 we substitute  $\Lambda(x) = \mathcal{R}(x) - 2\mathcal{R}(x-1) + \mathcal{R}(x-2)$ , where  $\mathcal{R}$  denotes the ramp function. We obtain eighty one terms, each of which is a product of four ramp functions. Using  $\mathcal{R}\left(\frac{1}{2}x\right) = \frac{1}{2}\mathcal{R}(x)$ , we can write each term in the integrand as a scalar fraction of:

$$I = \int_a^b \mathcal{R}(w+t_0) \mathcal{R}(w+t_1) \mathcal{R}(w+t_2) \mathcal{R}(w+t_3) dw.$$

This simplifies to a polynomial times four Heaviside distributions that we can evaluate analytically:

$$\begin{aligned} I &= \int_a^b \prod_{i=1}^4 (w+t_i) \mathcal{H}(w+t_i) dw \\ &= \int_c^b \prod_{i=1}^4 (w+t_i) dw. \end{aligned}$$

where  $c = \min(b, \max(a, \max(-t_i)))$  and one can compute the integral of this polynomial analytically.

### 5.1 Simplification of the Linear Kernel

An alternative method of deriving the linear kernel can be obtained through a geometric argument.

All of the polyhedra discussed in Section 3 are convex and therefore may be described as the intersection of a set of half spaces. Further, each face is matched by a parallel antipodal face; this is due to the group structure of the lattice. If a point  $\mathbf{a}$  is in the lattice and vector  $\mathbf{b}$  takes it to a neighbor then  $\mathbf{a} + \mathbf{b}$  is in the lattice; then the group property enforces  $\mathbf{a} - \mathbf{b}$  be a point in the lattice as well, hence the antipodal symmetry. As a consequence the polyhedra lend themselves to a convenient description in terms of the level sets of piecewise linear functions.

Consider the rhombic dodecahedron, for example. Each of its twelve rhombic faces can be seen to lie centered on the edges of a cube such that the vector from the center of the cube to the center of its edge is orthogonal to the rhombic face placed on that edge.

So the interior of the rhombic dodecahedron that encloses the unit cube in this way can be described as the intersection of the twelve half spaces

$$\pm x \pm y \leq \sqrt{2}, \quad \pm x \pm z \leq \sqrt{2}, \quad \pm y \pm z \leq \sqrt{2}. \quad (9)$$

Now consider the pyramid with apex at the center of the polyhedron and whose base is a face  $f$  with unit outward normal  $\hat{\mathbf{n}}_f$ . Notice that for any point  $\mathbf{p}$  within this pyramid, the scalar product  $\mathbf{p} \cdot \hat{\mathbf{n}}_f$  is larger than  $\mathbf{p} \cdot \hat{\mathbf{n}}_{f'}$ , where  $\hat{\mathbf{n}}_{f'}$  is the outward normal for any other rhombic face  $f'$ . Thus if we define a function

$$\begin{aligned} \phi : \mathbb{R}^3 &\longrightarrow \mathbb{R} \\ \phi : (\mathbf{p}) &\longmapsto \max_{\hat{\mathbf{n}}_f} \mathbf{p} \cdot \hat{\mathbf{n}}_f, \end{aligned} \quad (10)$$

its level sets are rhombic dodecahedra. We can use the axial symmetries of the half spaces (9) to write the function (10) for the rhombic dodecahedron in the compact form

$$\phi(x, y, z) = \max(|x| + |y|, |x| + |z|, |y| + |z|).$$

For a fixed  $s$ , all the points in the space with  $\phi(x, y, z) < s$  are the interior of the rhombic dodecahedron,  $\phi(x, y, z) = s$  are on the rhombic dodecahedron and  $\phi(x, y, z) > s$  are on the outside of the rhombic dodecahedron. Therefore for all  $s \geq 0$  the function  $\phi(x, y, z)$  describes concentric rhombic dodecahedra that are growing outside from the origin linearly with respect to  $s$ .

Using this fact, one can derive the function that is two at the center of the rhombic dodecahedron and decreases linearly to zero at the vertices, similar to the linear kernel described in Equation 3, to be:

$$L_{RD}(x, y, z) = 2 \max(0, 1 - \max(|x| + |y|, |x| + |z|, |y| + |z|)). \quad (11)$$

## 6 Results and Discussion

The optimality properties of the BCC sampling imply that the spectrum of a Cartesian sampled volume matches the spectrum of a BCC sampled volume with 29.3% fewer samples [11]. On the other hand, given equivalent sampling density per volume, the BCC sampled volume outperforms the Cartesian sampling in terms of information captured during the sampling operation. Therefore, in our test cases, we are comparing renditions of a Cartesian sampled dataset against renditions of an equivalently dense BCC sampled volume as well as against a BCC volume with 30% fewer samples.

In order to examine the reconstruction schemes discussed in this paper, we have implemented a ray-caster to render images from the Cartesian<sup>3</sup> and the BCC sampled volumetric datasets. The normal estimation, needed for shading, was based on central differencing of the reconstructed continuous function both in the Cartesian and BCC case. Central Differencing is easy to implement and there is no reason to believe that it performs any better or worse than taking the analytical derivative of the reconstruction kernel [15].

We have chosen the synthetic dataset first proposed in [12] as a benchmark for our comparisons. The function was sampled at the resolution of  $40 \times 40 \times 40$  on the Cartesian lattice and at an equivalent sampling on the BCC lattice of  $32 \times 32 \times 63$ . For the sake of comparison with these volumes a 30% reduced volume of  $28 \times 28 \times 55$  samples on the BCC lattice along with a volume of 30% increased sampling

<sup>3</sup>In order to ensure fair comparison of Cartesian vs. BCC sampling we should compare our new interpolation filters with filters based on the octahedron of first neighbors cell (see Section 3.1). However, tri-linear filtering is the common standard in volume rendering and since tri-linear filters are superior to the octahedron based filters, we will compare our new filters to the tensor-product spline family instead.

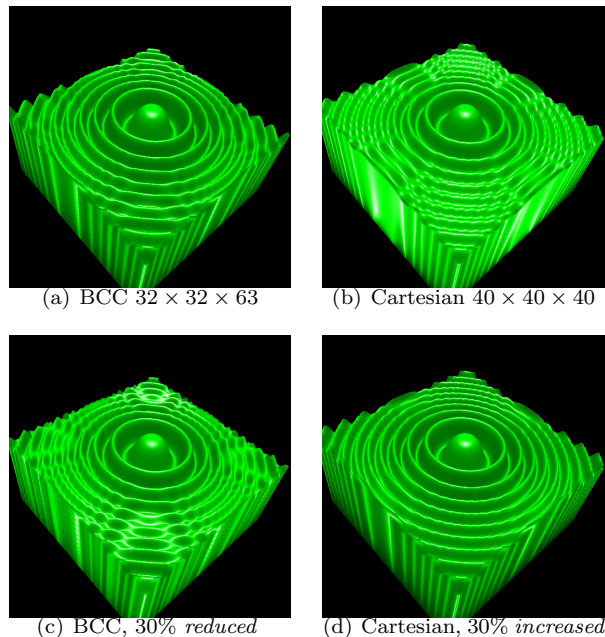


Figure 4: Comparison of BCC and Cartesian sampling, cubic reconstruction

resolution of  $44 \times 44 \times 44$  for the Cartesian sampling was also rendered. The images in Figure 4 are rendered using the cubic box spline on the BCC sampled datasets and the tri-cubic B-spline on the Cartesian sampled datasets. The images in Figure 5 document the corresponding error images that are obtained by the angular error incurred in estimating the normal (by central differencing) on the reconstructed function. The gray value of 255 (white) denotes the angular error of  $30^\circ$  between the computed normal and the exact normal.

The optimality of the BCC sampling is apparent by comparing the images Figure 4(a) and Figure 4(b) as these are obtained from an equivalent sampling density over the volume. While the lobes are mainly preserved in the BCC case, they are smoothed out in the case of Cartesian sampling. This is also confirmed by their corresponding error images in Figure 5. The image in Figure 4(c) is obtained with a 30% reduction in the sampling density over the volume of the BCC sampled data while the image in Figure 4(d) is obtained with a 30% increase in the sampling density over the volume of the Cartesian sampled data. One could match the quality in Figure 4(c) with Figure 4(b) and the Figure 4(d) with the Figure 4(a), this pattern can also be observed in the error images of Figure 5. This matches our predictions from the theory of optimal sampling.

We also examined the quality of the linear kernel on this test function. The renditions of the test function using the linear kernel on the BCC lattice and tri-linear interpolation on the Cartesian lattice are illustrated in Figure 6.

Since 98% of the energy of the test function is concentrated below the 41st wavenumber in the frequency domain [12], this sampling resolution is at a critical sampling rate and hence a lot of aliasing appears during linear interpolation. We doubled the sampling rate on each dimension and repeated the experiment in Figure 7. Figure 8 demonstrates the errors in the normal estimation. Due to the higher sam-

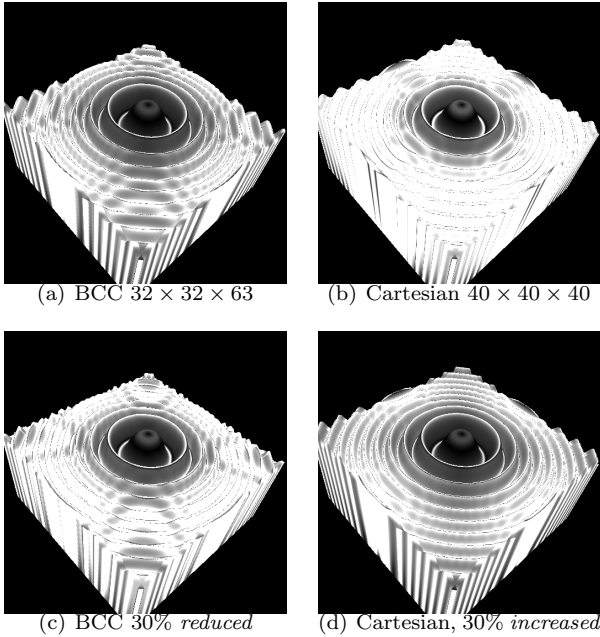


Figure 5: Angular error of the computed normal versus the exact normal, cubic reconstruction. Angular error of  $30^\circ$  mapped to white

pling density, the errors in normal estimation are considerably decreased; hence we have mapped the gray value 255 (white) to  $5^\circ$  of error.

Renditions of the Marschner-Lobb function with this higher sampling resolution using cubic reconstruction and the corresponding error images are illustrated in Figure 9 and in Figure 10.

Throughout the images in Figure 4 through Figure 10, one can observe the optimality of the BCC sampling compared to the Cartesian sampling.

Real volumetric datasets are scanned and reconstructed on the Cartesian lattice; there are filtering steps involved in scanning and reconstruction that tune the data according to the Cartesian sampling so the spectrum of the captured data is anti-aliased with respect to the geometry of the Cartesian lattice. Therefore, the ultimate test of the BCC interpolation can not be performed until there are optimal BCC sampling scanners available.

However, for examining the quality of our reconstruction filters on real world datasets we used a Cartesian filter to resample the Cartesian datasets on the BCC lattice. While prone to the errors of the reconstruction before resampling, we have produced BCC sampled volumes of the tooth and the UNC brain datasets with 30% reduction in the number of samples. The original tooth volume has a resolution of  $160 \times 160 \times 160$  and the BCC volume after the 30% reduction has a resolution of  $113 \times 113 \times 226$ ; similarly for the UNC dataset, the original Cartesian resolution of  $256 \times 256 \times 145$  was reduced by 30% to the BCC resolution of  $181 \times 181 \times 205$ . The result of their rendering using the linear and the cubic box spline in the BCC case and the tri-linear and tri-cubic B-spline reconstruction in the Cartesian case is illustrated in Figure 11 and Figure 12. These images were rendered at a  $512^2$  resolution on an SGI machine with sixty four 1.5GHz Intel Itanium processors running Linux.

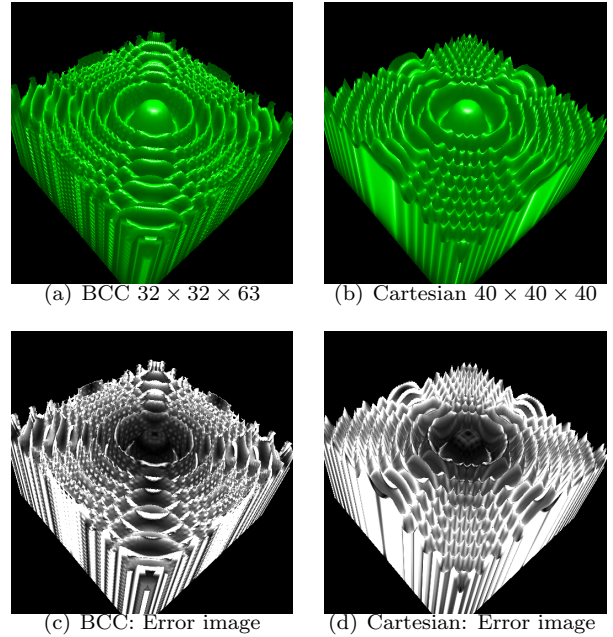


Figure 6: Comparison of BCC and Cartesian sampling, linear interpolation. In the error images, angular error of  $30^\circ$  mapped to white

## 7 Conclusion

In this paper we have derived an analytic description of linear and cubic box splines for the body centered cubic (BCC) lattice. Using geometric arguments, we have further derived a simplified analytical form of the linear box spline in Equation 11, which is simple and fast to evaluate (simpler than the trilinear interpolation function for Cartesian lattices).

Further we have also derived the analytical description of the Fourier transform of these novel filters and by demonstrating the number of vanishing moments we have established the numerical order of these filters. We believe that these filters will provide the key for a more widespread use of BCC sampled lattices.

Our images support the theoretical results of the equivalence of Cartesian lattices with BCC lattices of 30% fewer samples.

## 8 Future Research

As we have obtained the linear interpolation filter from projection of the tesseract, we can obtain odd order splines by successive convolutions of the linear kernel (or alternatively – projecting a tesseract which is the tensor product of higher order one-dimensional splines). However, the even order splines and their analytical forms do not seem to be easily derived. We are currently investigating this case.

The ease of deriving the frequency response of these interpolation filters lends itself to a thorough error analysis on this family.

Further, the computation of the cubic box spline in Equation 5 currently entails the evaluation of 81 terms. This makes the evaluation of the cubic kernel computationally expensive. We are currently investigating simplifications similar to that of the linear kernel discussed in Section 5.1.

Except for the first order box spline, the spline family are approximating filters, hence research on exact interpolatory

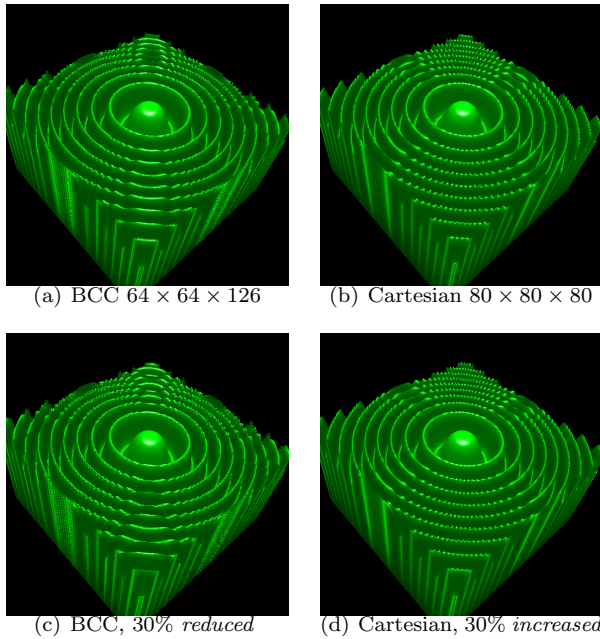


Figure 7: Linear interpolation at a higher resolution

filters, similar to those of Catmull-Rom for the BCC lattice is being explored.

## References

- [1] A.V.Oppenheim and R.W.Schafer. *Discrete-Time Signal Processing*. Prentice Hall Inc., Englewoods Cliffs, NJ, 1989.
- [2] Gerald Burns. *Solid State Physics*. Academic Press Inc., 1985.
- [3] Ingrid Carlbom. Optimal filter design for volume reconstruction and visualization. In *Proceedings of the IEEE Conference on Visualization 1993*, pages 54–61, October 1993.
- [4] H. Carr, T. Theußl, and T. Möller. Isosurfaces on optimal regular samples. In *Joint Eurographics - IEEE TCVG Symposium on Visualization*, pages 39–48, May 2003.
- [5] H. Carr, T. Möller, and J. Snoeyink. Simplicial subdivisions and sampling artifacts. In *Proceedings of the IEEE Conference on Visualization*, pages 99–106, October 2001.
- [6] J.H Conway and N.J.A. Sloane. *Sphere Packings, Lattices and Groups*. Springer, 3rd edition, 1998.
- [7] Carl deBoor, K Höllig, and S Riemenschneider. *Box splines*. Springer Verlag, 1993.
- [8] D. E. Dudgeon and R. M. Mersereau. *Multidimensional Digital Signal Processing*. Prentice-Hall, Inc., Englewood-Cliffs, NJ, 1st edition, 1984.
- [9] T.C. Hales. Cannonballs and honeycombs. *Notices of the AMS*, 47(4):440–449, April 2000.
- [10] T. Theußl, O. Mattausch, T. Möller, and E. Gröller. Reconstruction schemes for high quality raycasting of the body-centered cubic grid. *TR-186-2-02-11, Institute of Computer Graphics and Algorithms, Vienna University of Technology*, December 2002.
- [11] Thomas Theußl, Torsten Möller, and Eduard Gröller. Optimal regular volume sampling. In *Proceedings of the IEEE Conference on Visualization 2001*, pages 91–98, Oct. 2001.
- [12] Steve R. Marschner and Richard J. Lobb. An evaluation of reconstruction filters for volume rendering. In R. Daniel Bergeron and Arie E. Kaufman, editors, *Proceedings of the IEEE Conference on Visualization 1994*, pages 100–107, Los

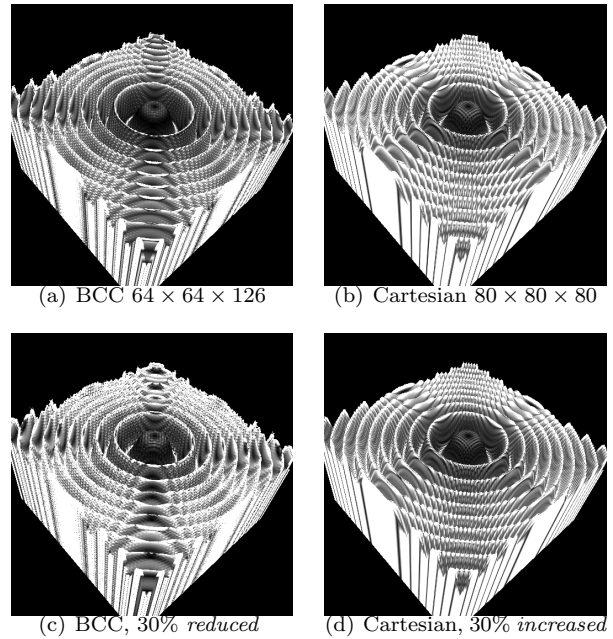


Figure 8: Angular error images for linear interpolation at a higher resolution. Angular error of  $5^\circ$  mapped to white (255)

Alamitos, CA, USA, October 1994. IEEE Computer Society Press.

- [13] R.M. Mersereau. The processing of hexagonally sampled two-dimensional signals. *Proceedings of the IEEE*, 67(6):930–949, June 1979.
- [14] Don P. Mitchell and Arun N. Netravali. Reconstruction filters in computer graphics. In *Computer Graphics (Proceedings of SIGGRAPH 88)*, volume 22, pages 221–228, August 1988.
- [15] Torsten Möller, Raghu Machiraju, Klaus Mueller, and Roni Yagel. A comparison of normal estimation schemes. In *Proceedings of the IEEE Conference on Visualization 1997*, pages 19–26, October 1997.
- [16] Torsten Möller, Klaus Mueller, Yair Kurzion, Raghu Machiraju, and Roni Yagel. Design of accurate and smooth filters for function and derivative reconstruction. *Proceedings of the 1998 Symposium on Volume Visualization*, pages 143–151, October 1998.
- [17] D. P. Petersen and D. Middleton. Sampling and reconstruction of wave-number-limited functions in  $N$ -dimensional Euclidean spaces. *Information and Control*, 5(4):279–323, December 1962.
- [18] R.G.Keys. Cubic convolution interpolation for digital image processing. *IEEE Trans. Acoustics, Speech, and Signal Processing*, 29(6):1153–1160, December 1981.
- [19] B.Kumar S.C.Dutta Roy. *Handbook of Statistics*, volume 10, chapter Digital Differentiators, pages 159–205. Elsevier Science Publishers B. V., North Holland, 1993.
- [20] Gilbert Strang and George J. Fix. A Fourier analysis of the finite element variational method. *Construct. Aspects of Funct. Anal.*, pages 796–830, 1971.
- [21] Van De Ville, D., Blu, T., M. Unser, W. Philips, I. Lemahieu, and R. Van de Walle. Hex-splines: A novel spline family for hexagonal lattices. *IEEE Transactions on Image Processing*, 13(6):758–772, June 2004.

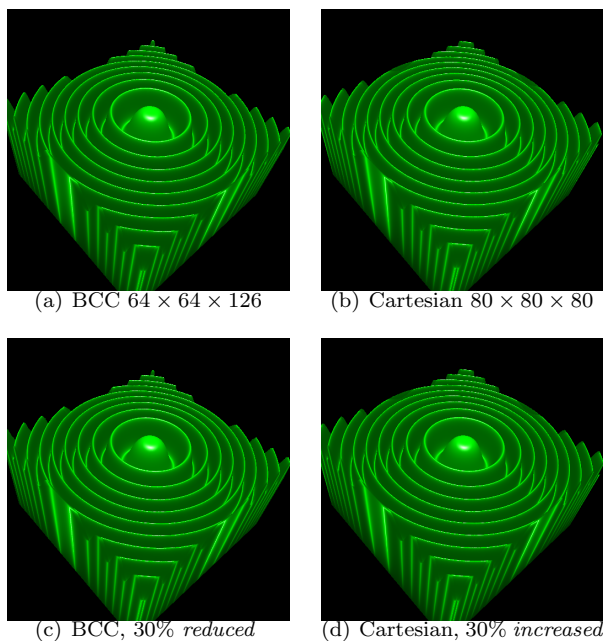


Figure 9: The cubic reconstruction at a higher resolution

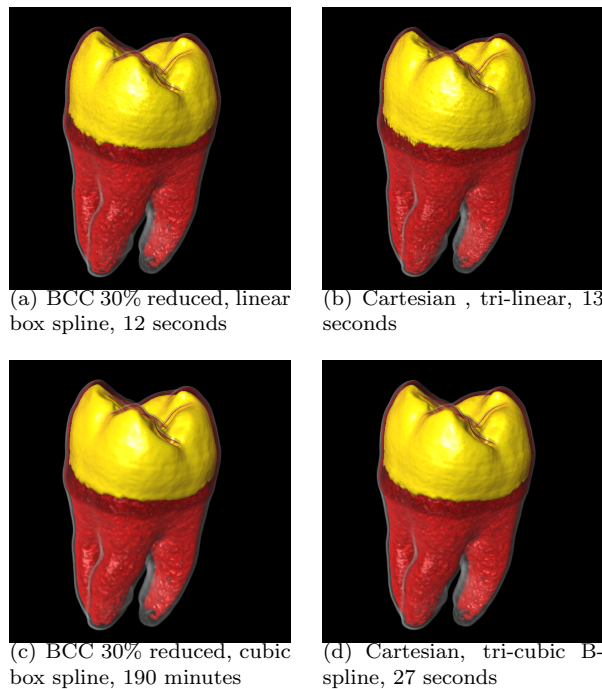


Figure 11: The tooth dataset

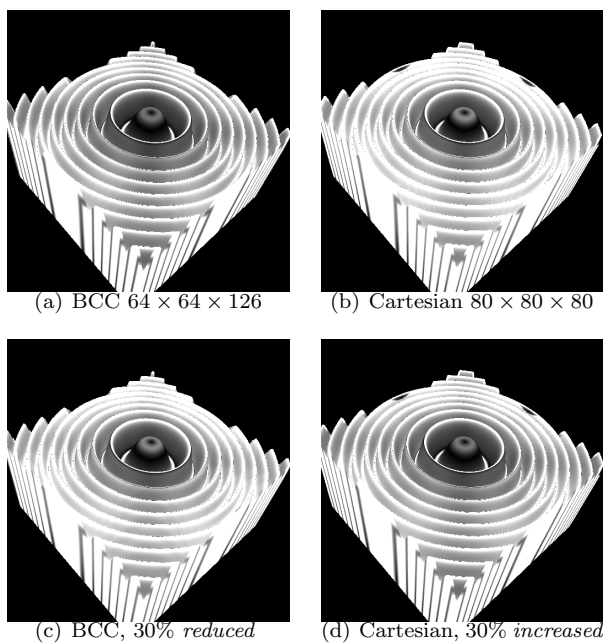


Figure 10: The error images in the cubic reconstruction at a higher resolution. Angular error of  $5^\circ$  mapped to white

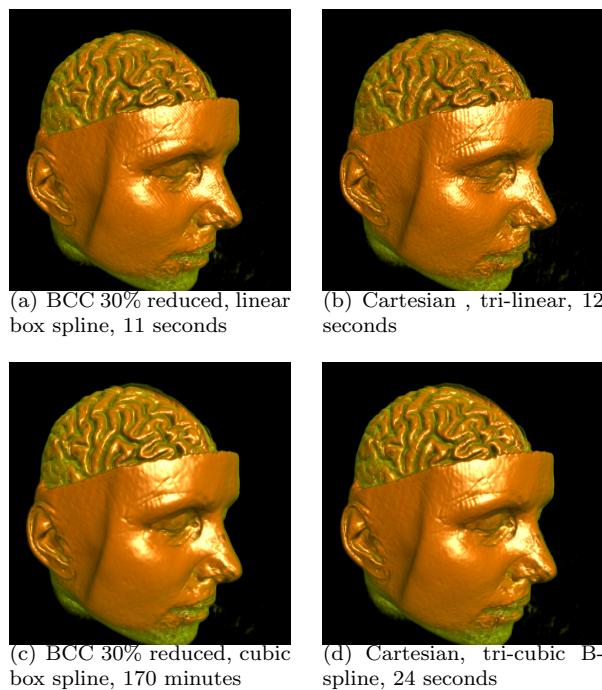


Figure 12: The UNC dataset